International Journal of Heat and Mass Transfer 51 (2008) 5182–5191

Contents lists available at ScienceDirect

International Journal of Heat and Mass Transfer

journal homepage: www.elsevier.com/locate/ijhmt

Three-dimensional laminar flow and heat transfer in a parallel array of microchannels etched on a substrate

Justin D. Mlcak [a], N.K. Anand [a,*], Michael J. Rightley [b]

[a] Department of Mechanical Engineering, Texas A&M University, College Station, TX 77843-3123, United States
[b] Sandia National Laboratories, Albuquerque, NM, United States

ARTICLE INFO

Article history:
Received 27 September 2007
Received in revised form 3 April 2008
Available online 12 June 2008

Keywords:
Microchannel
Conjugate heat transfer
SIMPLE
Repeating array

ABSTRACT

Heat transfer and laminar fluid flow in an array of parallel microchannels etched on a silicon substrate with water as the circulating fluid was studied numerically. The fluid region consisted of a microchannel with a hydraulic diameter of 85.6 μm and aspect ratios ranging from 0.10 to 1.0. A constant heat flux of 90 W/cm^2 was applied to the $y = H$ face of the computational domain, which simulates thermal energy generation from an integrated circuit. Generalized transport equations were discretized and solved in three dimensions for velocities, pressure, and temperature. The SIMPLE algorithm [S.V. Patankar, Numerical Heat Transfer and Fluid Flow, Hemisphere, New York, 1980] was used to link pressure and velocity fields, and a thermally repeated boundary condition was applied in the lateral direction to model the repeating nature of the geometry. The numerical results for apparent friction coefficient and convective thermal resistance at the channel inlet and exit closely matched the experimental data in the literature for the case of 0.32 aspect ratio. Apparent friction coefficients were found to increase linearly with Reynolds number. Inlet and outlet thermal resistance values monotonically decreased with increasing Reynolds number and increased with aspect ratio.

1. Introduction

Over two and a half decades ago, microchannels emerged as a potential solution for dissipating thermal energy from densely packed integrated circuitry. Proposals and research indicated that high heat fluxes could be dissipated by a fluid passing through microchannels that offer an increased surface area to volume ratio. In the early 1980s, Tuckerman and Pease [2] reported that a microchannel heat sink could dissipate as much as 790 W/cm^2 with a 71 °C mean fluid temperature rise. Because of increasing heat flux from a higher density of integrated circuitry, there is an increasing need for more research into microchannel design, performance, and application.

While some microchannel devices are well understood, a fundamental understanding of the thermal and hydraulic performance of microchannel devices is lacking. Without this detailed knowledge, cooling microchannels may not be designed for optimum heat transfer or pressure drop. Not only does this affect the design of the microchannel device, but this also impacts the design of external pumping and thermal management systems.

In this work, fluid flow and heat transfer are modeled for water flowing in 110 parallel rectangular microchannels etched on a silicon substrate with an 86.6 μm hydraulic diameter and 100 μm pitch as shown in Fig. 1a–d. The geometries modeled in this study are similar to the case studied experimentally by Kawano et al. [3]. Five additional aspect ratios ranging from 0.10 to 1.0 were considered in this work.

Existing experimental data and analytical models for heat transfer and fluid flow sometimes differ greatly from one another, and sometimes the results are nearly identical [4]. Over the past two decades, at least a dozen experimental and physical parameters have been proposed that are thought to have a strong influence on the performance of these cooling systems [5]. Combining all of these factors into a viable predictive simulation is a daunting task. Clearly, widely-accepted theories are needed to explain the behavior of fluid flow and heat transfer at the micro-scale.

Bontemps [5] explained the usefulness of the Knudsen number (Kn) as a validity indicator of the continuum hypothesis for fluid in a channel of specified length. The Knudsen number is the ratio of the molecular mean free path and the channel characteristic length.

The mean molecular free path is approximately 8 nm for liquid water, and the characteristic length of the microchannels for the present study was 21.7 μm, yielding a value for Kn of 3.7×10^{-4} and clearly justifying a continuum assumption. Fig. 2 illustrates various fluid flow models with respect to Knudsen number [5]. As shown by the point of interest for liquid water in the Figure, the Navier–Stokes equations and no-slip boundary conditions apply to the current work. The same is not true for gas microflows

* Corresponding author. Tel.: +1 979 845 5633; fax: +1 979 845 3081.
E-mail address: nkanand@tamu.edu (N.K. Anand).

0017-9310/$ - see front matter © 2008 Elsevier Ltd. All rights reserved.
doi:10.1016/j.ijheatmasstransfer.2008.04.032

Nomenclature

A_c	channel cross-sectional area, m^2
C	distance between the bottom of the substrate and the channel central axis, m
c_p	specific heat at constant pressure, J/(kg K)
D_h	hydraulic diameter, m
f	friction factor
h	channel height, m
H	computational domain height (y-direction), m
k	thermal conductivity, W/(m K)
Kn	Knudsen number
L	channel length, m
Nu	Nusselt number
p	pressure, Pa
Po	Poiseuille number (fRe)
P_s	channel perimeter, m
q''	heat flux, W/m^2
Re	Reynolds number
R_t	thermal resistance
S	surface along channel perimeter
T	temperature, K
T_m	mean (bulk) temperature, K
T_w	average wall temperature, K
u	x-direction velocity component, m/s
$\vec{V}$	velocity vector
v	y-direction velocity component, m/s
W	computational domain width (z-direction), m
w	z-direction velocity component, m/s
w_c	channel width, m
x	x coordinate direction
y	y coordinate direction
z	z coordinate direction

Greek

α	channel aspect ratio (w/h)
Δ	length of control volume side, m
μ	viscosity, N s/m^2
ρ	density, kg/m^3

Subscripts

app	apparent
f	fluid
m	mean

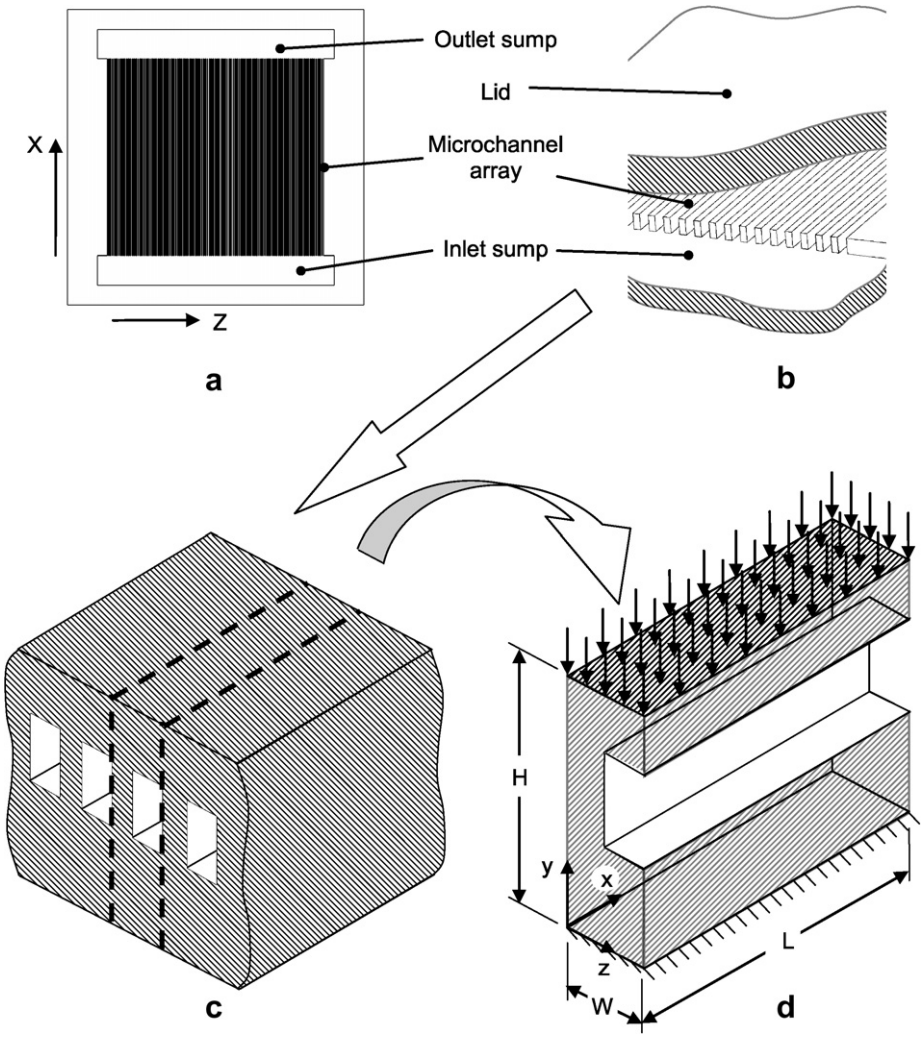

Fig. 1. Repeating microchannel geometry showing: (a) top view, (b) three-dimensional cut away of microchannel array, (c) repeating microchannel, and (d) single computational domain used for simulating entire array.

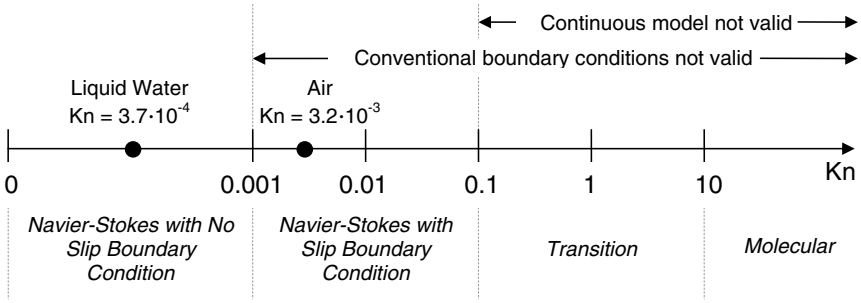

Fig. 2. Assumed fluid flow model as a function of Knudsen number (Kn) (adapted from [5]).

in the same channel size where Kn is 3.24×10^{-3}, a value that is in the range of slip boundary conditions.

Mala and Li [6] reported larger friction factors than predicted from a reduction of Navier–Stokes, and the difference became larger with decreasing microtube diameter. These effects were attributed to an early transition to turbulence and a change in tube surface roughness. Wu and Cheng [7] measured friction factor and Nusselt number for laminar water flow in trapezoidal microchannels. Surface roughness, hydrophilic properties (solid/liquid contact angle), and channel geometries were varied. Both friction factor and Nusselt number were reported to increase linearly with Reynolds number between $Re = 100$ and $Re = 600$, which differs from fully developed Navier–Stokes and energy equation predictions.

Several investigators attempt to explain differences between experimental results and theory. Agostini et al. [8] detailed the importance of obtaining a very low uncertainty when measuring the dimensions of mini and microchannels. An example illustrated that a 3% uncertainty on channel width and height results in a friction factor uncertainty of 21%. Additional sources of possible experimental error may include: increased pressure drop due to singular pressure losses at the entrance and exit of flow manifolds [8] and hydrodynamic development [9]; excessive thermocouple junction size (on the order of the channels themselves) [5]; temperature rises in the fluid that are not properly resolvable with existing thermometry [5]; and trapped gas in liquid microchannel flows that adversely affect pressure drop (tends to increase) and Nusselt number (tends to decrease) [10].

In some cases, theoretical predictions closely approximate experimental results. Xu et al. [11] measured friction factor for hydraulic diameters ranging from 30 to 344 μm and Reynolds numbers ranging from 20 to 4000. For this set of experiments, theoretical predictions matched the recorded data when error ranges from experimental uncertainty were considered.

Previously, attempts had been made to validate the experimental results against hydrodynamically and thermally fully developed Navier–Stokes and energy equation predictions, but Toh et al. [9] were among the first to successfully model developing flows and conjugate heat transfer. Thermal resistances and friction factors obtained from the numerical results of Toh et al. [9] closely matched experimental data.

Another numerical study by Fedorov and Viskanta [12] solved for fluid flow and conjugate heat transfer in three dimensions for a 57 μm × 180 μm channel using the SIMPLER algorithm [1] with Reynolds number ranging from 50 to 400. Results were compared against existing experimental data. Nearly all numerical predictions for friction factor and thermal resistance matched the experimental data when experimental uncertainty was considered.

Bontemps [5] presented a figure that shows $Nu_{exp}/Nu_{classical}$ and $f_{exp}/f_{classical}$ as a function of published year from 1990 to 2004. The curves in this plot converged toward a value of 1 as the years approached 2004. Bontemps extrapolated from this result that classical (Navier–Stokes and energy equations) theories may be applicable on the micro-scale [5].

The present work differs from that of Fedorov and Viskanta [12] by using a thermally repeated boundary condition along the z-boundaries; by using the SIMPLE algorithm instead of the SIMPLER algorithm [1]; and by obtaining solutions for channels with different aspect ratios.

The main objective of this work was to model three-dimensional velocity, pressure, and temperature distributions in a parallel array of microchannels etched on a silicon substrate. Also, a thermally repeated boundary condition was implemented to model the repeating microchannel array. Numerical results were compared to available experimental data [3], and channel aspect ratios between 0.1 and 1.0 of the same hydraulic diameter and pitch were considered.

2. Model formulation

The case considered in this work is a single-phase forced convective flow of water in an array of parallel microchannels etched on a silicon substrate. In this problem, the forced convection component is large, and since the density of liquid water is roughly invariant with temperature, at least in the range of interest here, mixed convection effects were not considered.

The experimental investigation that served as an origin for the present numerical model was the work of Kawano et al. [3]. The microchannel device was constructed by etching 110 identical channels centered onto a 15 mm by 15 mm by 450 μm thick silicon substrate. Each channel was 57 μm in width and 180 μm in height, and the pitch of the channels was 100 μm. After the etching, the channels were covered with a 450 μm thick silicon cover plate which was etched with holes for connection to the sumps. While the exact method of cover plate attachment was not documented, the two silicon pieces were joined by a molecular diffusion technique [3].

Thin film Fe–Ni thermocouples were created at the inlet and exit of the device by sputtering. These thermocouples allowed for measurement of the solid silicon temperature near the channel inlet and outlet. In this study, measurements from these thermocouples were compared to numerical predictions of temperature in the solid at the same location.

Kawano et al. [3] controlled water flow by means of a flow meter and a valve for Reynolds number ranging from approximately 50 to 400. A heating device which provided a constant heat flux of 90 W/cm^2 was mated to the side of the microchannel device opposite the flow inlet.

In the present work, additional microchannel geometries were considered which had the same number of channels (1 1 0) and pitch. A cross-section of one repeating section of the microchannel

geometry and the associated boundary conditions are illustrated in Fig. 3. Actual lengths for the different geometries modeled are given in Table 1. The experimental geometry of Kawano et al. [3] is equivalent to the $\alpha = 0.32$ case in Table 1. Each case listed in the table has a hydraulic diameter equal to 86.6 μm. As shown in Fig. 3, the constant heat flux was applied to the silicon substrate at $y = H$, and a thermally insulated condition was applied at $y = 0$. Although no insulation was in place at $y = 0$ during the experiment, this was the location of a holder, and Kawano et al. assumes that this location was thermally insulated [3].

The Navier–Stokes and energy equations were solved for the geometries listed in Table 1. Flow was considered to be steady, incompressible, three-dimensional and laminar. Thermo-physical properties of the solid substrate were treated as constants. Fluid properties were held constant throughout the computational domain, and the values were dependent on average of outlet and inlet mean fluid temperatures obtained from an energy balance.

The Navier–Stokes, energy, energy source term, and continuity equations for steady-state, incompressible flows in the absence of gravitational forces are given in Eqs. (1)–(3), respectively

$$\vec{V}\cdot\nabla\left(\rho\vec{V}\right) = -\nabla p + \nabla\cdot\left(\mu\nabla\vec{V}\right), \tag{1}$$

$$\vec{V}\cdot\nabla\left(\rho c_p T\right) = \nabla\cdot\left(k\nabla T\right), \tag{2}$$

$$\rho\left(\nabla\cdot\vec{V}\right) = 0. \tag{3}$$

These equations were solved using the finite volume method and the SIMPLE algorithm of Patankar [1]

The solution to Eqs. (1)–(3) was dependent upon the application of boundary conditions, which are graphically depicted in Fig. 3 and are the same for all geometries listed in Table 1. The velocity boundary conditions were: zero velocity at all y- and z-domain boundary surfaces; uniform x-velocity for liquid at the channel inlet according to Eq. (4); zero y- and z-velocities at channel inlet; and zero velocity in the solid region at $x = 0$

$$u|_{x=0,\text{fluid inlet}} = \frac{Re\mu_{\text{fluid}}}{\rho_{\text{fluid}} D_h}. \tag{4}$$

Thermal boundary conditions included: uniform fluid and solid temperature of 20 °C at the channel inlet; constant heat flux of 90 W/cm^2 at $y = H$ for all x and z; thermally insulated at $y = 0$; and a thermally repeated boundary condition at $z = 0$ and $z = W$. The mathematical definition of the thermally repeated boundary condition is given by Eqs. (5) and (6)

$$T_{z=0} = T_{z=W}, \tag{5}$$

$$\left(-k\frac{\partial T}{\partial z}\right)_{z=0^+} = \left(-k\frac{\partial T}{\partial z}\right)_{z=W^-} \tag{6}$$

A thermally repeated boundary condition is one in which the temperatures at both z-boundaries of the computational domain are equal, and the heat flux leaving the $z = W$ side of the computational boundary is equal to the heat flux entering the $z = 0$ side of the computational boundary for a fixed value of y. Due to the repeated nature of the geometry, heating, and flow conditions the repeated thermal boundary conditions prevail in a channel somewhere in the interior of the array [13]. A channel subjected to such a thermally repeated condition in the cross-stream direction was the focus of this work.

The basic channel and solid dimensions for the case of $\alpha = 0.32$ were similar to those used to validate Fedorov and Viskanta's code [12]. Fedorov and Viskanta simulated a different geometry in which the fluid channel was centered in the computational domain and the insulated boundary condition was applied in the repeating direction contrasting to the thermally repeating boundary condition of the present study. The implementation of a thermally repeated boundary condition differs from the non-thermally repeating cases by using a cyclic line-by-line solving algorithm known as the cyclic tri-diagonal matrix algorithm (CTDMA), whereas normal line-by-line solvers use a tri-diagonal matrix algorithm (TDMA).

Table 1
Dimensions of channel geometries for cases of different aspect ratio

Aspect ratio α (w/h)	Channel height, hv/(μm)	Channel width, w_c/(μm)
0.10	476	47.6
0.25	217	54.1
0.32	180	57.0
0.50	130	64.9
0.75	101	75.8
1.0	86.6	86.6

The channel length and domain length are 10 mm for all cases of aspect ratio.

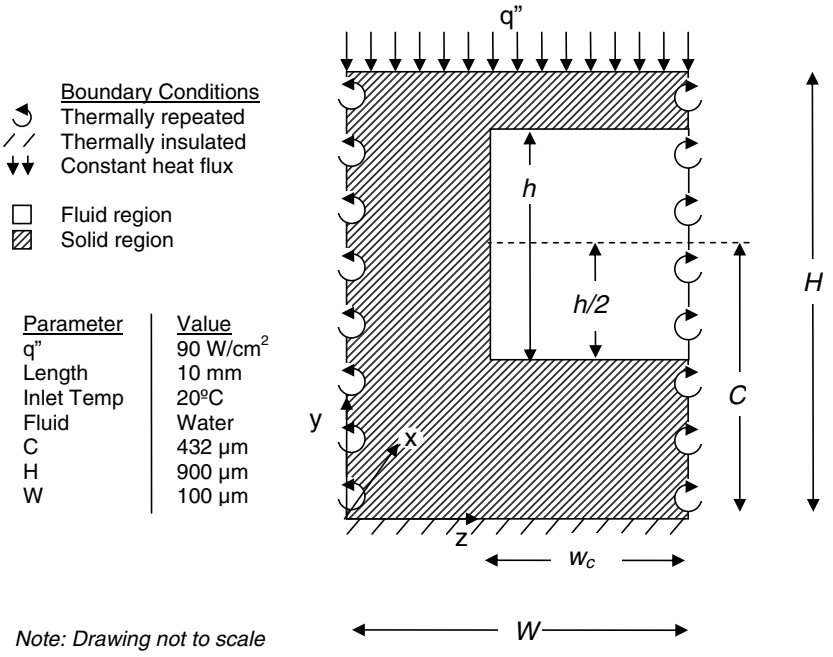

Fig. 3. Y–Z cross-section and boundary conditions for the rectangular microchannel under study.

The numerical solution was not dependent upon the conditions at the outflow boundary, and no information was carried from the outflow boundary into the computational domain. The assumption was made that the flow was hydrodynamically and thermally fully developed at the channel outlet, which is considered valid due to the large value of the channel length to hydraulic diameter ratio (115).

The conjugate heat transfer problem was solved by including the solid and liquid regions in the computational domain for temperature, pressure, and velocity. The solid region was given an arbitrarily large viscosity value to effectively drive the velocity in the region to a near-zero value, and the thermal conductivity in the solid region was equal to the temperature-invariant thermal conductivity of the solid material.

The average of the inlet and outlet mean fluid temperatures was used to determine fluid properties. The outlet temperature was calculated from an energy balance within the computational domain, as shown in Eq. (7).

$$T|_{x=L} = \frac{q''LW}{\rho h w c_p u|_{x=0}} + T|_{x=0} \tag{7}$$

Other than the high viscosity value, the only property that differed in the solid versus the fluid regions was the thermal conductivity. The thermal conductivity used in the solid was 148 W/mK for single crystal silicon.

The convergence of the code was declared when the residuals for pressure, temperature, and the three coordinate velocities reached arbitrarily small epsilon values of 10^{-5}, 5×10^{-8}, and 10^{-7}, respectively.

3. Grid independence

The code was validated by comparing fully developed *fRe* and *Nu* values to the analytical solutions of Shah and London [14]. Eqs. (8)–(12) provide definitions for *fRe*, $f_{app}Re$, *Nu*, mean wall temperature $T_{w,m}$, and mean fluid temperature, T_m. After the validation tests were performed, the cases shown in Table 1 were modeled

$$\mathrm{Po} = f \cdot Re = \frac{2D_h^2}{u_m \mu_{fluid}} \frac{\partial p}{\partial x}, \tag{8}$$

$$\mathrm{Po}_{app} = f_{app} \cdot Re = \frac{2\Delta p D_h^2}{u_m L \mu_{fluid}}, \tag{9}$$

$$Nu = \frac{q'' D_h}{k_{fluid}(T_{w,m} - T_m)}, \tag{10}$$

where

$$T_{w,m}(x) = \frac{1}{P_s} \int_S T_w(y,z)\,dS, \tag{11}$$

$$T_m(x) = \frac{1}{u_m A_c} \int_A u(y,z) T(y,z)\,dy\,dz. \tag{12}$$

Since exact solutions were not known for each of these cases, it was important to perform a grid independence study for the highest Reynolds number in the worst geometry scenario. The aspect

Table 2
Tabulated results of the grid independence study

Case	X	Y	Z	Number of nodes	% diff	$f_{app}Re$	% diff	$R_{t,outlet}$	% diff
1	100	44	8	35200		80.397		7.164×10^{-2}	
2	105	54	9	51030	44.97	82.504	2.62	7.191×10^{-2}	0.368
3	110	60	11	72600	42.27	83.791	1.56	7.203×10^{-2}	0.175
4	115	70	13	104650	44.15	84.674	1.05	7.218×10^{-2}	0.197
5	120	84	15	151200	44.48	85.702	1.21	7.232×10^{-2}	0.201
6	123	90	16	177120	17.14	86.020	0.371	7.237×10^{-2}	0.0622
7	125	105	17	223125	25.97	86.051	0.0360	7.231×10^{-2}	0.0801

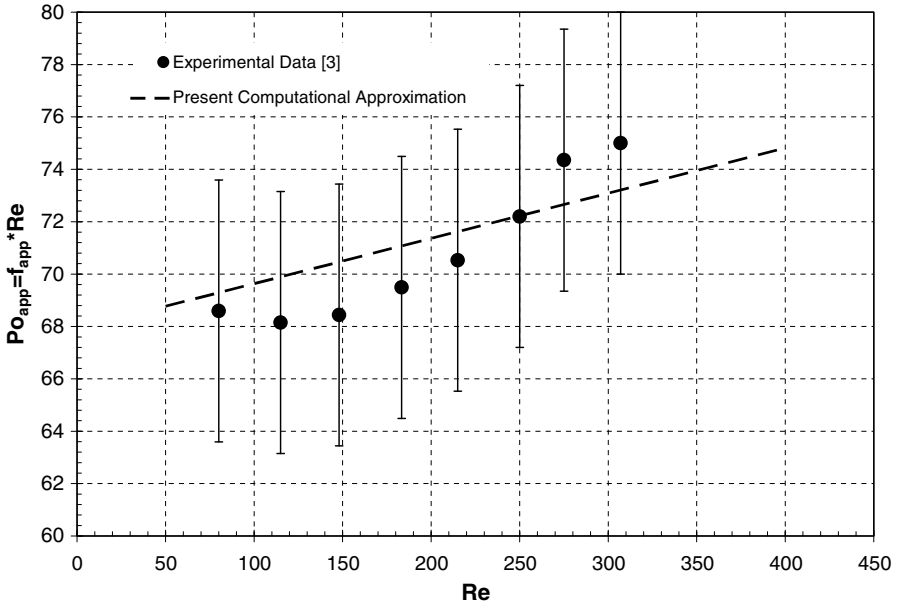

Fig. 4. Comparison of present computational results of apparent friction coefficient with the experimental data of Kawano et al. [3], α=0.32.

ratio of 0.10 was chosen to be the worst case geometry because it has the largest cross sectional flow area and because of large velocity gradients in the narrow z-direction of the channel. The values of two variables were monitored to declare grid independence. The $f_{app}Re$ value as defined in Eq. (9) was used to monitor behavior of the velocity and pressure fields for the entire channel length, and the outlet thermal resistance value, $R_{t,\ outlet}$, as defined by Eq. (13) was used to monitor the behavior of the temperature field

$$R_{t,outlet} = \frac{T_{w,outlet} - T_{f,inlet}}{q''}. \tag{13}$$

The thermal resistance of Eq. (13) is basically a sum of the conduction and convection thermal resistances. For a case of constant thermal conductivity in the substrate and variable flow rate, a low thermal resistance value indicates a high convection coefficient between the substrate and the fluid. Conversely, high thermal resistance indicates relatively weak convective transport. The thermal resistance is also an indicator of maximum substrate temperature since the wall temperature at $y = H$ is used at the channel outlet, which is the location of the maximum substrate temperature.

For the case of constant flow rate and variable thermal conductivity in the substrate, a low thermal resistance indicates a high substrate thermal conductivity due to small temperature gradients, implying a relative insensitivity to fluid temperature. A high value of thermal resistance means that the substrate acts as an insulator (i.e., low k) indicating a significant difference between inlet fluid temperature and substrate temperature at the channel exit.

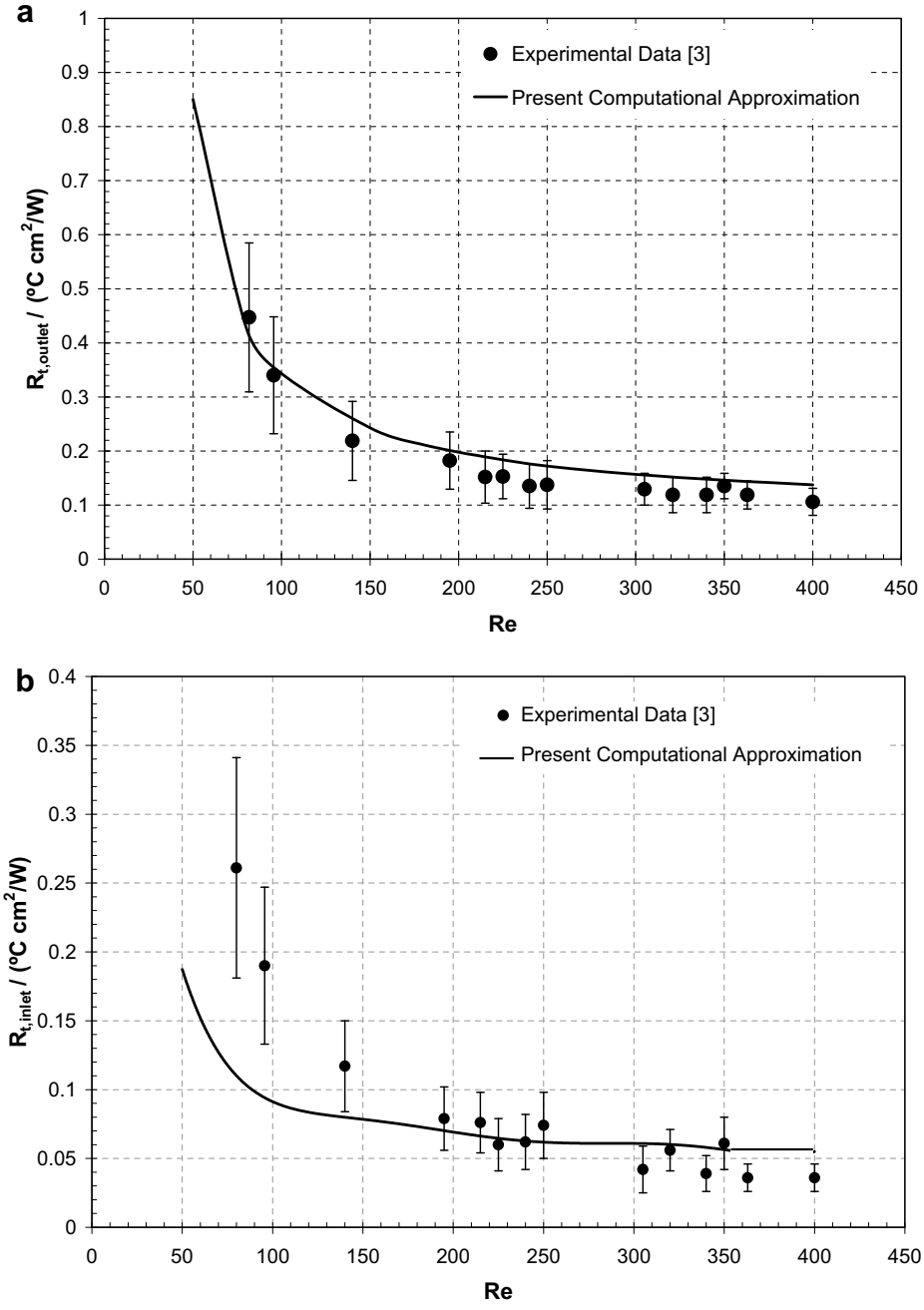

Fig. 5. Comparison of present computational results of convective thermal resistance with the experimental data of Kawano et al. [3], $\alpha = 0.32$ at (a) the channel exit and (b) the channel inlet.

Seven different non-uniform grid sizes were used in the grid independence study, and the results are shown in Table 2. According to the results, one can see that the percent differences between cases 5, 6, and 7 were very small. Therefore, case 5 was declared as grid independent.

Values of Δx, Δy, and Δz for case 5 were used to solve all of the other geometries of different aspect ratio. The first 100 nodes within the first 4 mm used a constant Δx value, and after the first 4 mm, Δx increased at a rate of 16% per node until the channel exit was encountered. Smaller control volumes were used in the first 4 mm so that all entry length effects are simulated correctly. The values of velocity, pressure gradient, and temperature gradient were constant after the entry region, so a coarser grid was used. Furthermore, velocities were zero within the solid region and temperature gradients were small compared to those in the fluid region justifying the use of a coarse grid in the solid region as well. Each solid control volume bordering the fluid region was given the same size as those in the fluid region so that accurate temperature and velocity gradients would be obtained. In case 5, ten solid control volumes were used in the y-direction and 5 solid control volumes were used in the z-direction.

4. Results and discussion

The basic equations were solved in a FORTRAN code using the SIMPLE algorithm [1] that solved for u, v, and w velocity fields, pressure field, and temperature field in three dimensions. The code was developed to solve these fields for each of the geometries listed in Table 1 as Reynolds number was varied between 50 and 400. Other values such as friction coefficient, mean temperature, and thermal resistance were calculated once the converged velocity, pressure, and temperature fields were obtained.

Another objective of this work was to compare the apparent friction coefficient and thermal resistance values obtained from

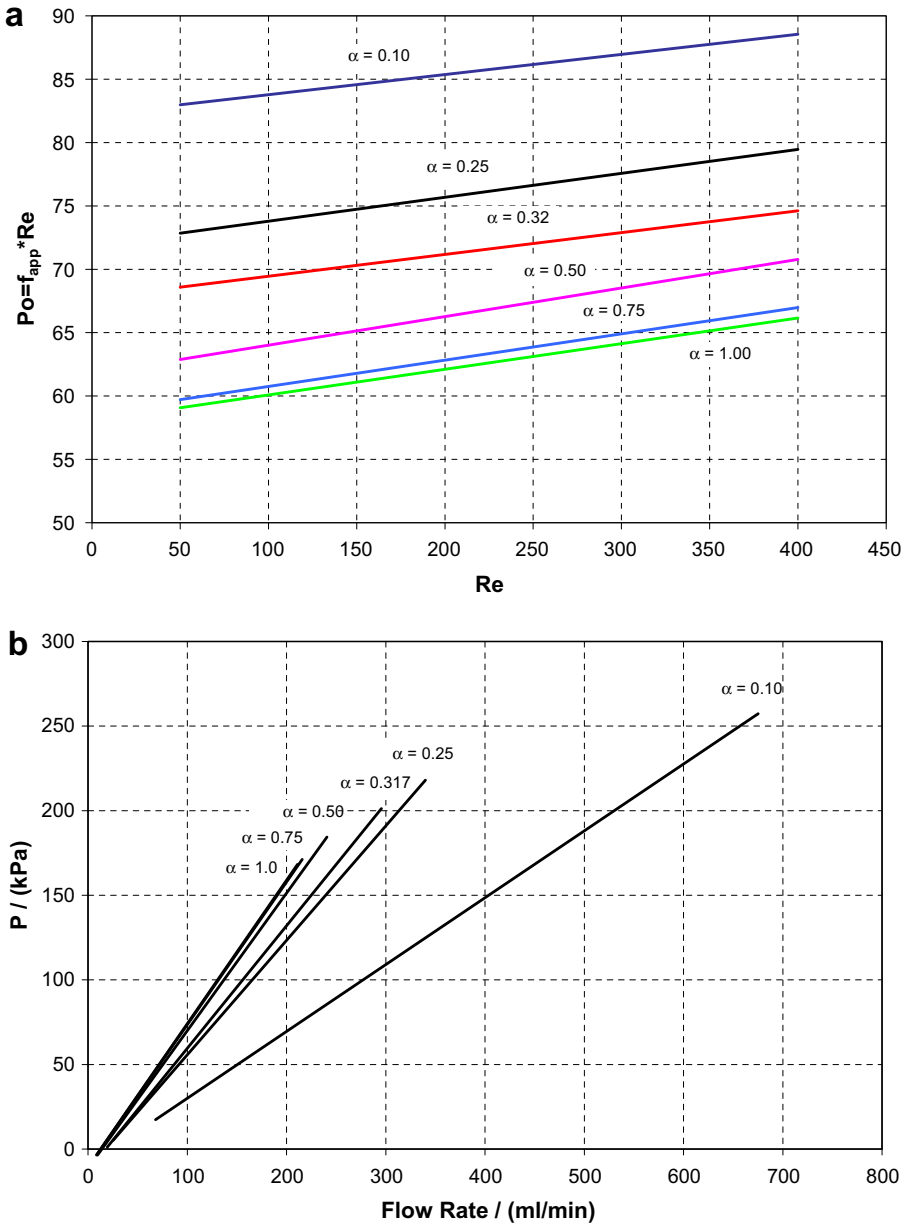

Fig. 6. Pressure drop data: (a) apparent friction factor versus Reynolds number for various aspect ratios and (b) system characteristic curves for the entire array of 110 parallel microchannels.

the computational results with available experimental data [3]. Equations for apparent friction coefficient and outlet thermal resistance are given by Eq. (9) and (13), respectively. The equation for inlet thermal resistance is given by Eq. (14), where $T_{w,inlet}$ is defined as the substrate temperature at $y = H$ at the channel inlet.

$$R_{t,inlet} = \frac{T_{w,inlet} - T_{f,inlet}}{q''}. \quad (14)$$

As the outlet thermal resistance is an indicator of thermal conductivity and convection coefficient, the inlet thermal resistance gives the same values on a different scale. For substrates with high thermal conductivity, $T_{w,inlet}$ and $T_{w,outlet}$ will have similar values, and the inlet and outlet resistances will be similar. Inlet and outlet resistances will be dissimilar for substrates with low thermal conductivity. Local convection coefficients are larger at the channel inlet than at the channel outlet because of entry effects, and the inlet thermal resistance conveys information about the convection coefficient. When more thermal energy is transferred to the fluid near the channel entrance, the substrate temperature near the channel entrance will decrease and the resistance will be lower. If less energy is transferred to or from the fluid near the channel entrance, the convection coefficient will be lower, which will increase the substrate temperature in this region as well as the resistance.

The comparison of apparent friction coefficient values between the present numerical study and the experimental work of Kawano et al. [3] is shown in Fig. 4. The comparison shows satisfactory agreement when experimental uncertainty is considered. The uncertainty range of these data was between 12% and 15%. In the range of Reynolds number studied, the variation of apparent friction coefficient was linear. This result differed from the fully devel-

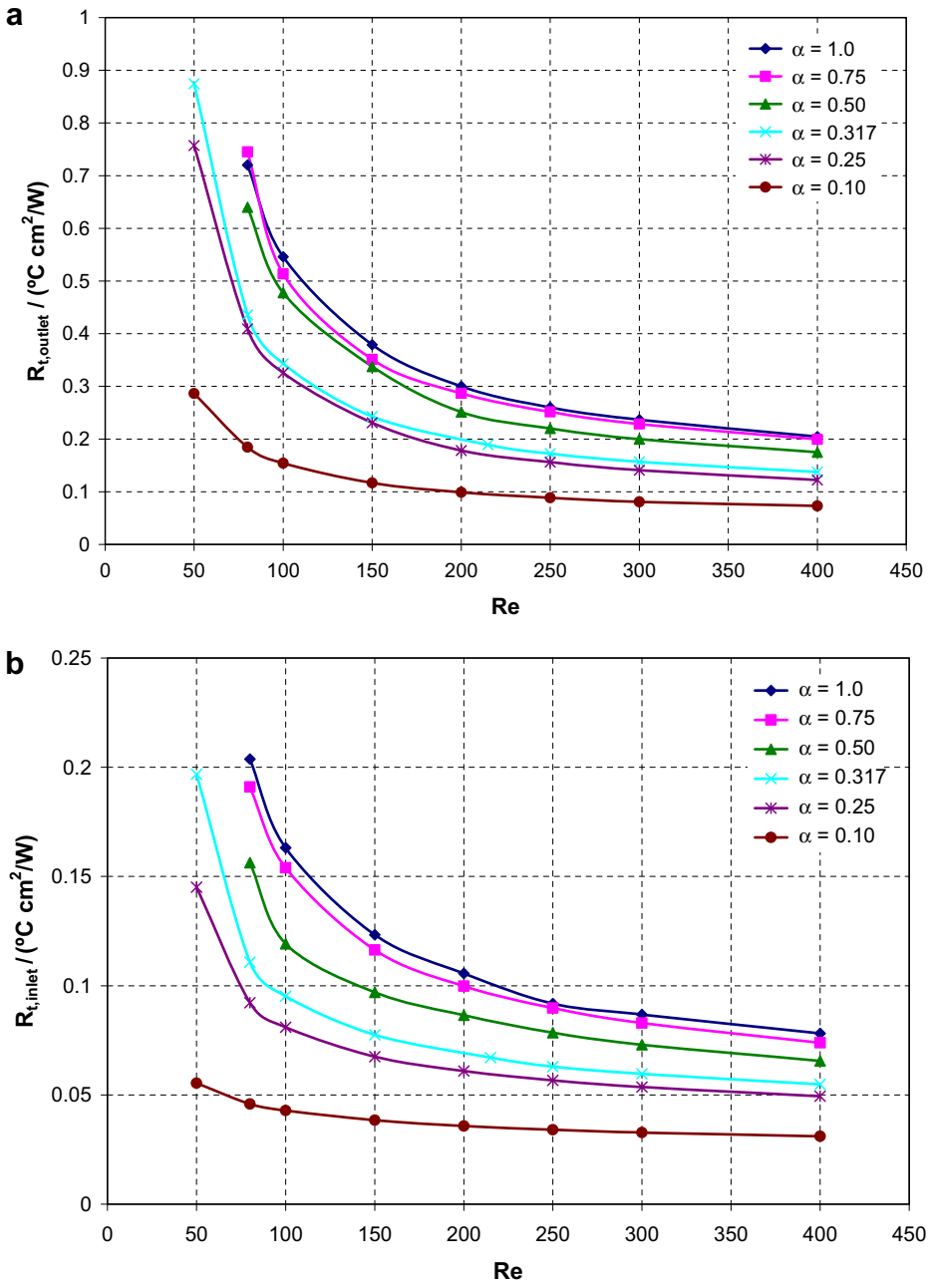

Fig. 7. Comparison of convective thermal resistance values for all cases of aspect ratio vs. Reynolds number at (a) the channel exit and (b) the channel inlet.

oped friction factor which is often used as a basis of comparison for laminar flows in microchannels. For the geometry considered, the fully developed flow friction coefficient was 69.2 [14], which does not match the data for Reynolds number above 250. Experimental data that do not match the fully developed flow friction coefficient are sometimes erroneously mistaken as an early transition to turbulence.

The linear increase of apparent friction coefficient with increasing Reynolds number can be explained by the increasing hydrodynamic entry length. Throughout the entry region, the flow was not developed and velocity gradients were large, leading to increased pressure drop. The increasing length of the entry region with Reynolds number resulted in a higher pressure drop across the channel. Local friction coefficient values at the channel exit were equal to the fully developed flow friction coefficient values for all Reynolds numbers in the laminar regime. It is satisfying to note that the present numerical results for apparent friction coefficient are nearly identical to the numerical results of [12,15], for the same geometry and boundary conditions.

Many experimental investigations of microchannels cited early transition to turbulence due to increasing friction coefficient with Reynolds number. For the range of Reynolds number considered, the entrance length was on the order of 10–20% of the channel length [14]. For higher Reynolds numbers within the laminar regime, the entrance region could extend beyond the channel length. This extension would bring about much higher laminar friction coefficients than those predicted by fully-developed laminar flow correlations.

Inlet and outlet convective thermal resistances are shown in Fig. 5. The predictions and experimental data for the resistances matched quite well when uncertainties were considered. The inlet thermal resistance differed for low Reynolds number flows, and the numerical model under-predicted the thermal resistances obtained experimentally. Qu et al. [15] suggested that this difference could be the result of heat loss to the upstream plenum because substrate temperatures were higher for low Reynolds number flows. In addition to the friction coefficient data, the numerically obtained results for convective thermal resistance in this study matched those obtained by [12,15] very closely. The thermal resistance values obtained in the present study slightly over-predicted those given by Fedorov et al. [12], whose results tended to fall in the ranges of the lower error bars shown in Fig. 5a.

As the apparent friction coefficient was compared with experimental data for an aspect ratio of 0.32 in Fig. 4, the apparent friction coefficients for all aspect ratios considered in this study are given in Fig. 6a. The slope of the $f_{app}Re$ vs. Re lines are nearly identical for each aspect ratio, and the curves only differ by translating to a higher $f_{app}Re$ value as the aspect ratio decreases. This makes intuitive sense because a fluid in a channel of smaller aspect ratio has higher velocity gradients than in channels with larger aspect ratios.

Using the data from the pressure fields to compute the apparent friction coefficients, the pressure drop across a single channel was determined for each flow rate and geometry. The flow rate per channel was multiplied by the number of channels in the array (1 1 0), and the system characteristic curves shown in Fig. 6b were produced. These characteristic curves could be used for selecting an appropriate pump for flows in the microchannel array.

For a given flowrate, the 0.10 aspect ratio channel had a lower pressure drop compared to all other channels. This is an important result because the 0.10 aspect ratio channel had the largest apparent friction coefficient but the lowest pressure drop for a given flow rate even though all channels had the same hydraulic diameter.

Fig. 7 shows values for thermal resistance at both the channel outlet and inlet for all Reynolds numbers and aspect ratios considered. This figure serves as a useful tool for understanding the variation of substrate temperature as a function of channel geometry and flow rate. At low flow rates, substrate temperatures can become very high as evidenced by the high values of thermal resistance at low Reynolds number and high aspect ratios. In these results, thermal resistance values for $Re = 50$ were not provided for aspect ratios 1.0, 0.75, and 0.50 because energy balance calculations indicated that the fluid would reach boiling temperatures. Boiling of liquid flows in microchannels has been the topic of many investigations, but it was not considered in the present study.

For high Reynolds numbers, the substrate temperatures became very close to the liquid inlet temperatures resulting in a low thermal resistance. This allows us to extrapolate that the microchannels can dissipate heat loads larger than 90 W/cm^2 for Reynolds

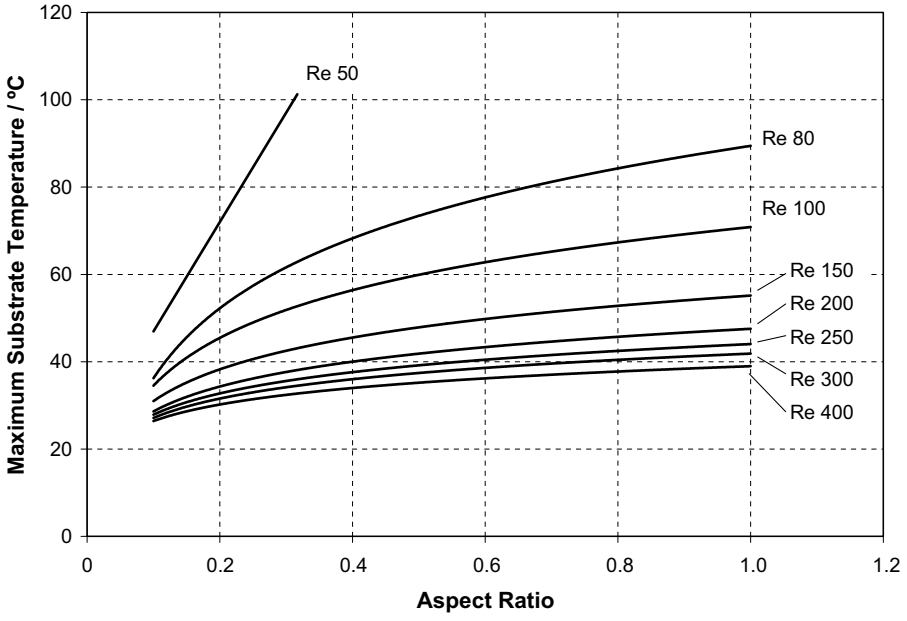

Fig. 8. Maximum silicon substrate temperature as a function of aspect ratio for Reynolds number ranging from 50 to 400.

number beyond 400 before substrate temperatures reach very high values.

Fig. 8 shows the maximum silicon substrate temperature for each case of Reynolds number and aspect ratio. This is an important consideration based on the proximal nature of the maximum temperature location and the heat source for which the device is intended. For small aspect ratios, the substrate temperature did not vary greatly as a function of Reynolds number. Larger aspect ratio channels had high maximum substrate temperatures for low values of Re. Increasing Reynolds number beyond 200 did not have a significant effect on reducing the maximum substrate temperature for any particular case of aspect ratio.

5. Conclusions

A numerical model was developed which simulated three dimensional fluid flow and heat transfer in a repeating section of a microchannel array etched on a silicon substrate. The conjugate nature of the heat transfer problem added complexity, and a thermally repeated boundary condition was implemented to model the repeating nature of the geometry. The three dimensional Navier–Stokes and continuity equations were solved using the SIMPLE algorithm, and once a converged velocity field was obtained, the three-dimensional convection–diffusion energy equations were solved simultaneously in both the solid and fluid regions. Rectangular microchannels with a hydraulic diameter of 86.6 μm were studied as aspect ratios varied from 0.10 to 1.0 and Reynolds numbers ranged from 50 to 400. In this study, the linearly increasing friction coefficient that was observed between Reynolds numbers 50 and 400 is a result of increased hydraulic entrance length. Friction coefficient values were also found to monotonically increase for aspect ratios approaching 0.10. The computational model developed in this study was validated by comparing friction factor and thermal resistance results with the experimental data of Kawano et al. [3] for the aspect ratio of 0.32. Because the solution of the energy equation was dependent upon velocity fields, the accuracy of the thermal resistance predictions of the experimental data lends credibility to both the fluid flow and thermal models. Values of inlet and outlet thermal resistance decreased for aspect ratios approaching 0.10, and for the same hydraulic diameter, inlet and outlet thermal resistances and friction coefficient values changed very little for aspect ratios larger than 0.50.

Acknowledgement

The authors would like to thank Sandia National Laboratories for funding this work and sharing their experiences in microfluidics with this research team.

References

[1] S.V. Patankar, Numerical Heat Transfer and Fluid Flow, Hemisphere, New York, 1980.
[2] B.D. Tuckerman, R.F.W. Pease, High-performance heat sinking for VLSI, IEEE Electr. Device Lett. EDL-2 (1981) 136–139.
[3] K. Kawano, K. Minakami, H. Iwasaki, M. Ishizuka, Development of micro channels heat exchanging, in: Proceedings of the ASME Heat Transfer Division: Application of Heat Transfer in Equipment, Systems, and Education, vol. 3, 1998, pp. 173–180.
[4] Y. Yener, S. Kakac, M. Avelino, T. Okutucu, Single-phase forced convection in microchannels: a state of the art review, in: S. Kakac, L.L. Vasiliev, Y. Bayazitoglu, Y. Yener (Eds.), Microscale Heat Transfer: Fundamentals and Applications, Series II, vol. 193, Springer, Dordrecht, Netherlands, 2004, pp. 1–24.
[5] A. Bontemps, Measurements of single-phase pressure drop and heat transfer coefficient in micro and minichannels, in: S. Kakac, L.L. Vasiliev, Y. Bayazitoglu, Y. Yener (Eds.), Microscale Heat Transfer: Fundamentals and Applications, Series II, vol. 193, Springer, Dordrecht, Netherlands, 2004, pp. 25–46.
[6] G.M. Mala, D. Li, Flow characteristics of water in microtubes, Int. J. Heat Fluid Flow 20 (1999) 142–148.
[7] H.Y. Wu, P. Cheng, An experimental study of convective heat transfer in silicon microchannels with different surface conditions, Int. J. Heat Mass Transfer 46 (2003) 2547–2556.
[8] B. Agostini, B. Watel, A. Bontemps, B. Thonon, Liquid flow friction factor and heat transfer coefficient in small channels: an experimental investigation, Exp. Therm. Fluid Sci. 28 (2004) 97–103.
[9] K.C. Toh, X.Y. Chen, J.C. Chai, Numerical computation of fluid flow and heat transfer in microchannels, Int. J. Heat Mass Transfer 45 (2002) 5133–5141.
[10] M.N. Sabry, Scale Effects on Fluid Flow and Heat Transfer in Microchannels, IEEE Trans. Compon. Pack Technol. 23 (2000) 562–567.
[11] B. Xu, K. Ooi, N.T. Wong, W.K. Choi, Experimental investigation of flow friction for liquid flow in microchannels, Int. Commun. Heat Mass Transfer 27 (2000) 1165–1176.
[12] A.G. Federov, R. Viskanta, Three-dimensional conjugate heat transfer in the microchannel heat sink for electronic packaging, Int. J. Heat Mass Transfer 43 (2000) 399–415.
[13] S.H. Kim, N.K. Anand, L.S. Fletcher, Free convection between series of vertical parallel plates with embedded line heat sources, ASME J. Heat Transfer 113 (1991) 108–115.
[14] R.K. Shah, A.L. London, Laminar Flow Forced Convection in Ducts, Academic Press, New York, 1978.
[15] W. Qu, I. Mudawar, Analysis of three-dimensional heat transfer in microchannel heat sinks, Int. J. Heat Mass Transfer 45 (2002) 3973–3985.